International Journal of Engineering Innovation & Research
Volume 5, Issue 1, ISSN: 2277 – 5668

A Numerical CFD Analysis on Supply Groove Effects in High Pressure, Open End Squeeze Film Dampers

Saeid Dousti, Ali Gerami, Majid Dousti

***Abstract* – In this paper, we address the supply groove depth and pressurization effects on the behavior of open end squeeze film dampers using numerical CFD approach. A steady state moving reference frame technique, rather than a full time transient one, is implemented in this study, which allows shortening the computation time significantly and to be able to examine more cases readily. Our findings show that significant fluid motion takes place in the supply groove causing its pressure to be varying mainly in circumferential direction and be lower than the supply pressure, in general. The supply holes configuration plays an important role in pressure profile both in groove and land region, especially when the supply groove is shallow. Mid land grooves may have significant dynamic contribution to squeeze film dampers despite their large depth. There exists an optimal supply groove depth which renders the squeeze film damper most effective. In higher rotational speeds and shallow supply grooves, negative pressure values and cavitation phenomenon appear which defeats the purpose of pressurization to a certain extent.**

***Keywords* – Squeeze Film, CFD, Supply Groove, Supply Hole.**

I. INTRODUCTION

For over a half-century, squeeze _lm dampers (hereafter SFD) have been adopted as a vibration attenuation tool in rotating machinery. In their simple structure, a lubricant _lm, trapped in the gap between the journal, usually the outer race of a roller element bearing, and the SFD housing, provides viscous damping and enhances the stability of the machine. An anti-rotation pin allows the journal only to translate, most commonly in a whirl motion [1, 2]. In some designs, axial ends of SFDs are sealed with the purpose of enhancing the load capacity, reducing cavitation, and reducing the ow rate [3, 4]. In aircraft engines, SFDs are the main damping source in the system. Gas turbine engines usually operate in very high temperature ranges, which may result in a drop in the lubricant viscosity, and consequently multi-solution behavior and jump phenomena [4]. Inayat-Hussain, Kanki, and Mureithi conducted a bifurcation study on axially sealed SFDs supporting rigid rotors and assumed simpli_ed long bearing solution [5]. Similar approach was applied by Dousti et al. to SFDs, centered with O-ring seals [4]. Zhao and Hahnby adopting the short bearing assumption studied open end SFDs [6]. These aformentioned papers (i.e., [4, 5, 6]) assumed π-film cavitation model and reported multi-solution operating zones and jump phenomenon. The cavitation and air ingestion was studied experimentally by Zeidan and Vance, who characterized the cavitation regimes in details [7, 8]. Boppa, Morrison, and Sekaran conducted a CFD study on low supply pressure SFDs and investigated the influence of the operating speed and the formed cavitation region[9]. Pressurization as a solution to the adverse effect of cavitation and jump phenomenon was addressed by Simandiri and Hahn [10]. They concluded that "significant unbalance force isolation is a practical possibility even with relatively high unbalance loading. In particular, with increased pressurization, the likelihood of bistable operation can be considerably reduced" [10]. Thus, high supply pressures up to 100(psi) = 7(bar) and higher are commonly practiced in aerospace applications. San Andres conducted a series of experimental studies on open end SFDs [1,3]. He reported significant inertia effects exhibited by the tested grooved SFDs which showed considerable differences compared to the classical predictions. Also, no pressure relief in the groove was evidenced, contrary to the general practiced knowledge.
This paper is conceived with the aim to study the groove depth effect in high pressure SFDs. This paper is structured in four main sections. In the first section, problem description and the details of the study cases are elaborated. The methodology and details of CFD approach is addressed in the second section. The results explained and discussed in the third section. The last section is the summary and conclusion.

II. PROBLEM DESCRIPTION

A three dimensional CFD analysis is conducted on a slightly modified SFD geometry of the test rig by san andres [1, 3]. Figure 1 shows the modeled lubricant region. Three supply holes (orifices), circumferentially 120_ apart, are contained in the journal and feed lubricant directly to the supply groove. This arrangement provides an axisymmetric lubrication condition. In this design, two end seal grooves are located close to the axial ends of the journal to allow piston ring seals installation. In this paper, open-end SFD configuration with the seal grooves included in the hydrodynamic zone, is considered. Additionally, two short lands beyond the end seal grooves are incorporated in the model, although they are not expected to have a big contribution. The original test rig utilizes a centering spring support characterized with Ks =18.7 MN/m stiffness. Based on San Andres [1,3], ISOVG2 oil at room temperature, T = 23_C, with the density and viscosity of ρ = 785(kgm-3) and μ=3.1(mPa.s) is used to simulate the high temperature operating conditions of gas turbine engines [3]. The land clearance to journal radius ratio of the modeled SFD is c/R =4e-3, which is larger than that of a typical hydrodynamic bearing ranging from 1.5e-3 to 2e-3. In this paper, in addition to the test rig's primary design, two SFDs with

International Journal of Engineering Innovation & Research
Volume 5, Issue 1, ISSN: 2277 – 5668

supply groove clearances of 3.3,1.2 (mm) are investigated, as well. Table 1 lists the geometric properties of the SFD illustrated in Fig. 1. As mentioned before, in aerospace applications, SFD pressurization is commonly applied to reach the ideal 2π film condition, and to avoid the adverse effects of cavitation. A high supply (inlet) pressure of Ps= 4.137(bar) is adopted in this study to present the lubrication condition in a real aircraft engine. Note that the experimental results by San Andres is obtained with 0:11(bar) for land clearance of 0.125(mm) [3] and 0:55(bar) for land clearance of 0.25(mm) [1] supplied to the test rig. Boppa et al. modeled lubricant as multiphase regime with 3% air entrained in the lubricant. Based on their comparison with experimental data, they concluded that a higher air entrainment percentage might be more realistic [9]. In this study, 4% air entrainment modeled as dispersed fluid and ideal gas is assumed to flow with the lubricant into the clearance domain via the three inlet holes and realizes the squeeze film.

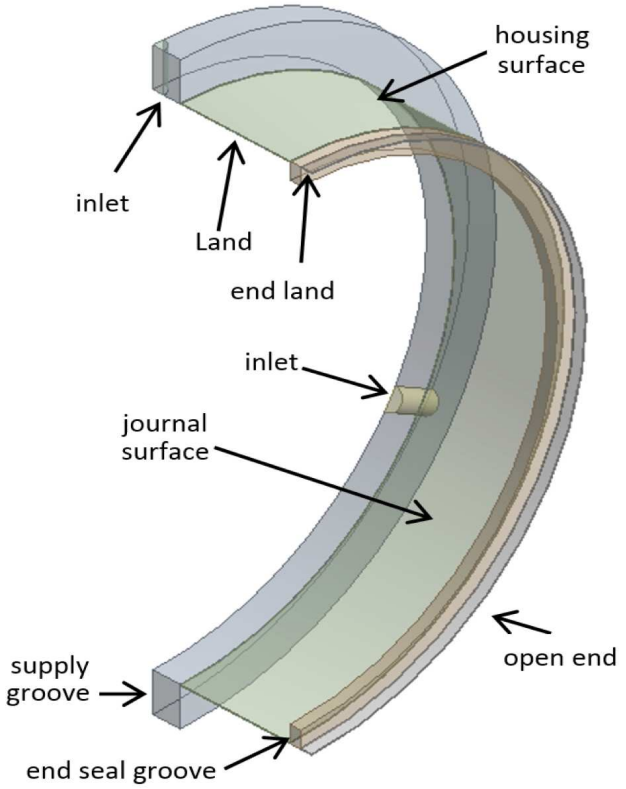

Fig.1. The geometry of squeeze film damper (a quarter of whole SFD)

III. CFD ANALYSIS

ANSYS-CFX v.14.5 (ANSYS Inc., Cannonsburg, PA) is used to perform the CFD study. In this CFD package, Reynolds averaged Navier-Stokes equations are solved via an element-based finite volume approach.

Table 1: Geometric parameters of modeled SFDs

Parameter	mm
Land clearance, cl	0.251
Journal radius, R	63:5
SFD length, L	73:66
Land length	25:4
End land length	2:54
Supply groove length	12:7
End seal grooves length	2:54
Supply groove clearance, GC	9:7; 3:3; 1:2
End seal grooves clearance	4:181
Supply hole radius	2:54

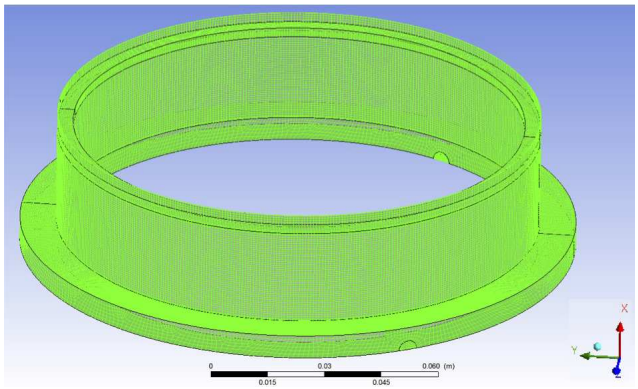

Fig. 2. Mesh grid of SFD half geometry, used in the CFD analysis.

$$\frac{\partial \rho}{\partial t}+\frac{\partial}{\partial x_j}(\rho U_j)=0 \quad (1)$$

$$\frac{\partial \rho U_i}{\partial t}+\frac{\partial}{\partial x_j}(\rho U_i U_j)=-\frac{\partial p}{\partial x_i}+\frac{\partial}{\partial x_j}\left[\mu_{eff}\left(\frac{\partial U_i}{\partial x_j}+\frac{\partial U_j}{\partial x_i}\right)\right] \quad (2)$$

where the effective viscosity is $\mu_{eff}=\mu+\mu_t$, $\mu_t=C_\mu \rho \frac{K^2}{\varepsilon}$ and C_μ is a constant in the equations above U_iS are velocity components, ρ is density, x_i is the coordinate components, and t is time. Unlike hydrodynamic bearing [11], with the lack of surface speed, the SFDs performance relies on the translation motion of the journal with negligible thermal effects, thus, isothermal assumption is justified. The κ and ε come directly from the differential transport equations for the turbulence kinetic energy and dissipation rate

$$\frac{\partial \rho k}{\partial t}+\frac{\partial}{\partial x_j}(\rho U_i k)=\frac{\partial}{\partial x_i}\left[\left(\mu+\frac{\mu_t}{\sigma_k}\right)\frac{k}{x_j}\right]+P_k-\rho\varepsilon \quad (3)$$

$$\frac{\partial \rho \varepsilon}{\partial t}+\frac{\partial}{\partial x_j}(\rho U_i \varepsilon)=\frac{\partial}{\partial x_i}\left[\left(\mu+\frac{\mu_t}{\sigma_k}\right)\frac{\varepsilon}{x_j}\right]-\rho\frac{\varepsilon^2}{k} \quad (4)$$

$$P_k=\mu_t\left(\frac{\partial U_i}{\partial x_j}+\frac{\partial U_j}{\partial x_i}\right)\frac{\partial U_i}{\partial x_j}-\frac{2}{3}\frac{\partial U_n}{\partial x_n}\left(3\mu_t\frac{\partial U_m}{\partial x_m}+\rho k\right) \quad (5)$$

Where σ_ε , σ_k are constants. In the above equations, k is Reynolds averaged kinetic energy of the turbulent eddies and "is dissipation. The second term in Eq. 5 is negligible for incompressible flows. The high resolution advection scheme is chosen and simulation convergence is

International Journal of Engineering Innovation & Research
Volume 5, Issue 1, ISSN: 2277 – 5668

user specified based on the root mean square (RMS) of the residuals less than 10-6 and invariance of the results with continual iterations. Due to the axial symmetry, half of the SFD geometry is analyzed with the supply groove axial wall modeled as a symmetric wall. The computational domain and grid are shown in Fig. 2. The inlet holes (orifices) are modeled as openings with Ps = 4.137 (bar) as the opening pressure and flow normal to the boundary, which allows for the back flow (partial or full) out of the domain via inlet holes in case of occurrence. A Moving Reference Frame technique with variant whirl speeds ranging between 50 - 250 (Hz) is used. The housing surface is modeled as counter rotating (stationary) wall. The journal surface is eccentric in Y direction with a value of 10% of the land clearance. To model the translation of the journal tangent to circular centered orbit trajectory (CCO), the surface is given a counter rotating wall velocity in the off-centered rotating reference frame. The adoption of CCO despite the axisymmetric design and inlet holes configuration makes it viable to assume that the variation of tangential and radial forces along the trajectory is negligible. Thus, a steady-state analysis is sufficient and is implemented. It is noteworthy to mention that the seal groove is a part of journal surface as is shown in Fig. 1. The axial end of the “end land" is modeled as outlet opening to ambient pressure. The mesh grid contains hexahedral structured elements, as is shown in Fig. 2, and utilizes 20 elements in the land and end land clearance region, and is comprised of 413162 nodes in total. A mesh independence study is carried out by increasing the division numbers in all directions and mainly in radial direction by 30%. As is depicted in Fig. 3, the force variation is less than 5%.

IV. Results and Discussion

The results reported in this section are obtained based on a CCO trajectory with a 0.0251(mm) radius equivalent to 0.1c, as shown in Fig. 4. As listed in Table 1, three supply groove clearances are examined. In addition to the default 4% air entrainment, a case with no air entrainment is considered. Five whirl speeds ranging between 50 and 250(Hz) with 50(Hz) increment are investigated.

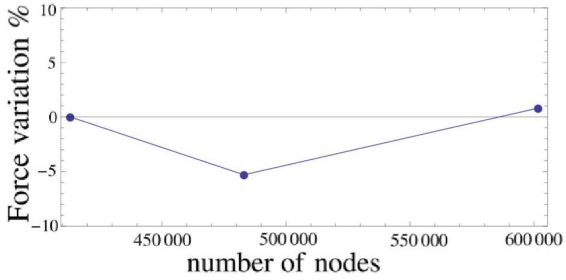

Fig. 3. Mesh independence study, the variation of tangential force w=50 Hz, and GC=3.3(mm), tangential force for the original mesh was $F_t = -113.116N$

V. Flow Pattern

Figure 5 exhibits the streamlines and flow patterns in the SFD. It can be seen that the inlet holes arrangement on the journal (and not as conventionally expected on the housing) results in a recirculation region with vortices that move in the opposite direction of the whirl motion and cause an axial flow close to the journal surface in the opposite direction of the one in land region. In the seal groove, similar to the supply groove, spiraling vortices are formed, which in contrast with those of the supply groove allow a “thru" region near the journal surface [12]. As is shown in Fig. 5b and discussed by San Andres and Delgado in [12], an artificial wall can be considered to separate the recirculation and thru regions.

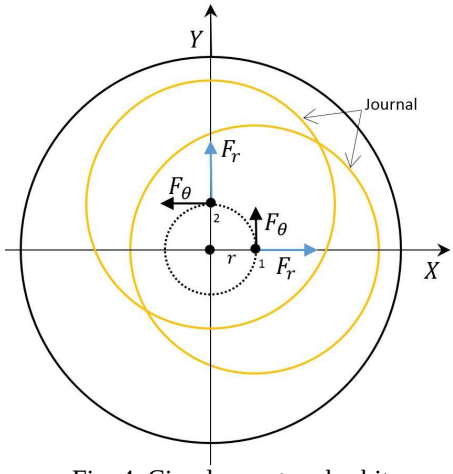

Fig. 4. Circular centered orbit

VI. Mass Flow Rate

Figure 6 presents the variation of mass flow rate for three different groove clearances versus whirl speed. It is shown that speed increase yields reduction in the flow rate. This is due to the higher pressure development in the supply groove for higher whirl speeds which opposes the flow rate supplied to SFD, as is illustrated in Figs. 7. By reducing the supply groove clearance, in general, a reduction in flow rate occurs. This trend is violated for higher speeds as GC decreases from 9.7(mm) to 3.3(mm).

VII. Pressure Field

The static pressure profile developed in SFD is discussed in this section, where all the reported values are gauge pressure. Figure 7 depicts the pressure contour plots of the inlet hole on “Y" axis for GC = 9.7 and GC = 1.2. It is shown that by decreasing the GC value, the maximum pressure location moves to the middle of the hole, and the hole edges experience lower pressures. Our findings also show that in spite of modeling the inlet holes as openings, no backflow via inlet holes occurs in any of the case studies. This characteristic can be justified by the high supply pressure value. It is also seen that the pressure

profiles of different inlet holes are almost the same for each case study.

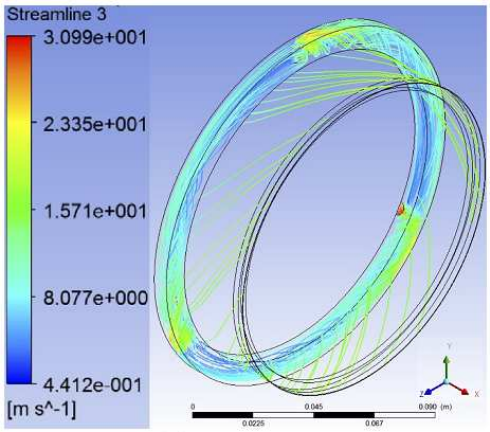

(a) 3D streamlines

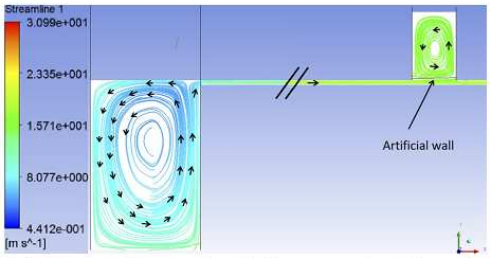

(b) 2D streamlines at $\theta = 180°$ cross section (the axial length is shortened)

Fig. 5. Typical 3D and 2D streamline plots

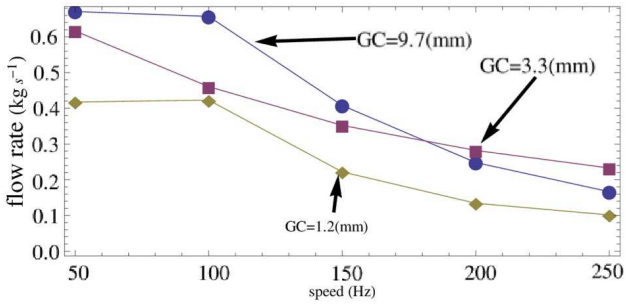

Fig. 6. Mass flow of sfd for a constant supply pressure, Ps = 4:137(bar)

The difference between the supply pressure and the pressure realized at the hole suggests that some of the supply energy is used to accelerate flow through the inlet holes. The difference between the supply pressure and the pressure realized at the hole suggests that some of the supply energy is used to accelerate flow through the inlet holes. The pressure profile contour plots of the supply groove are plotted in Fig. 8. It is observed that the supply holes split the circumference of the supply groove to three similar sectors. On these sectors, pressure decreases from one inlet hole to another as it accelerates in the direction of the whirl with almost no variation in the radial direction. This variation is more pronounced for shallower supply grooves. Also it can be seen that the average static pressure in the supply groove is less than 40% of the supply pressure due to the recirculation and flows in the groove. A wake region with low pressure is realized next to the inlet holes. The increase in the whirl speed intensifies the difference between maximum and minimum pressure values, i.e., peak to peak pressure, and negative pressure regions appear for ω> 200(Hz) resulting in cavitation phenomenon.

These observations reject the long lasting traditional perception that the supply groove region sustains a uniform pressure equal to the supply one independent of its geometry and the dynamic of the SFD. Also, it signifies the appearance of cavitation at high whirl speeds even with pressurization. This indicates that multi solution phenomenon associated with cavatation might yet occur even with pressurization. Figure 9 illustrates the pressure contour plots in the (vacant) seal groove. It can be seen that the pressure varies in circumferential direction majorly and in radial direction slightly.

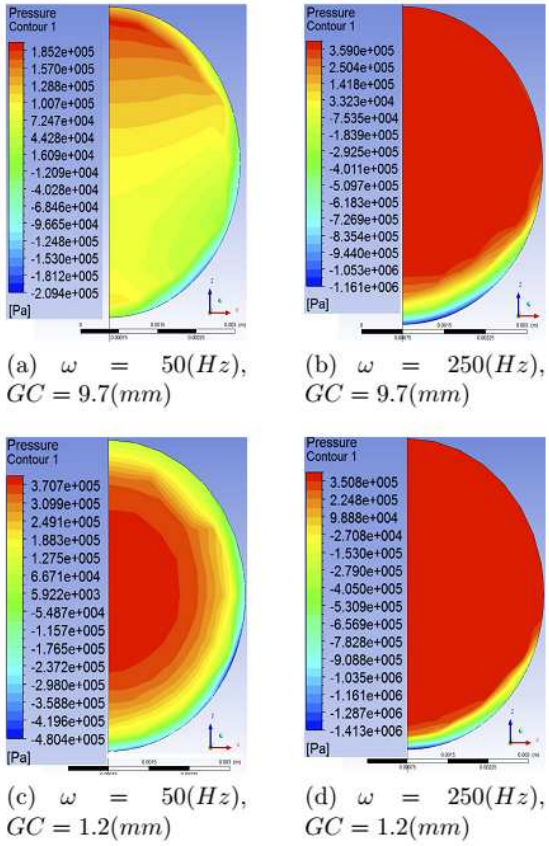

(a) $\omega = 50(Hz)$, $GC = 9.7(mm)$ (b) $\omega = 250(Hz)$, $GC = 9.7(mm)$

(c) $\omega = 50(Hz)$, $GC = 1.2(mm)$ (d) $\omega = 250(Hz)$, $GC = 1.2(mm)$

Fig. 7. Pressure contour plots of the “Y” coordinate inlet hole (based on Fig. 5a)

In higher whirl speeds, the variation in radial direction diminishes and regions of negative pressure appear. As such, higher velocities and stronger vortecies generated in the seal groove cavity at higher speeds result in a pressure drop at some portions of the journal surface due to Bernoulli effects. This large clearance area does not act similar to the thin squeeze film portion and flow pattern is more complicated in it. In Figs. 10-12, pressure profile in axial and circumferential directions are depicted for three GC.

International Journal of Engineering Innovation & Research
Volume 5, Issue 1, ISSN: 2277 – 5668

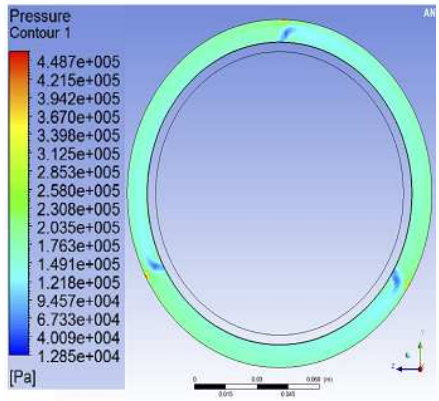

(a) $\omega = 50(Hz)$, $GC = 9.7(mm)$

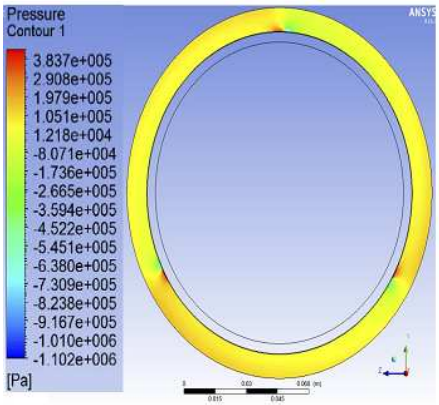

(b) $\omega = 250(Hz)$, $GC = 9.7(mm)$

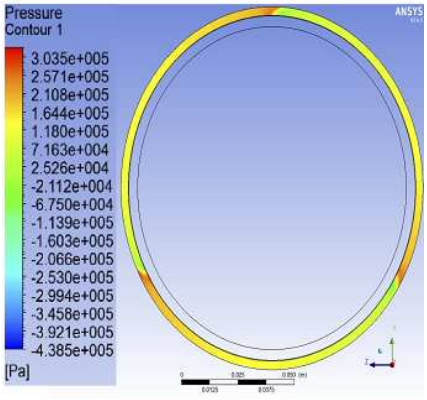

(c) $\omega = 50(Hz)$, $GC = 3.3(mm)$

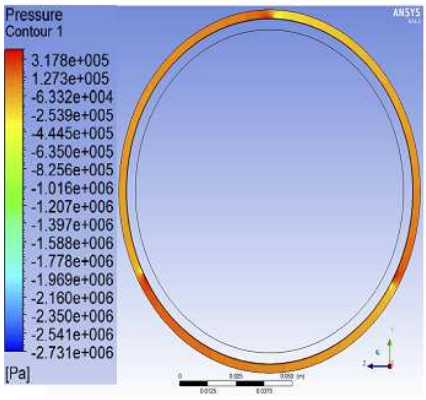

(d) $\omega = 250(Hz)$, $GC = 3.3(mm)$

Fig. 8. Pressure contour plots of the supply groove at x = 0 surface

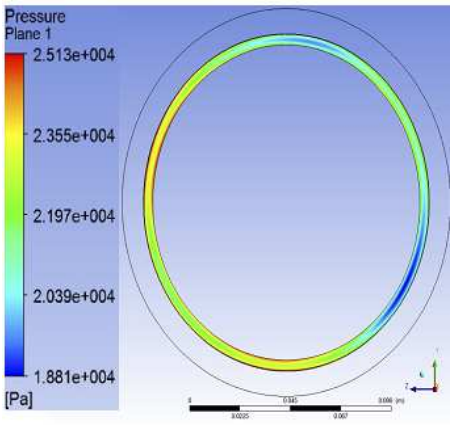

(a) $\omega = 50(Hz)$

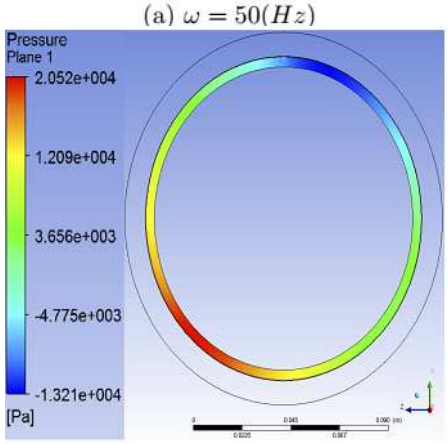

(b) $\omega = 250(Hz)$

Fig. 9. Pressure contour plots of the seal groove

and four whirl speed cases. Figures 10 and 11 are characterized with an almost constant pressure zone along the supply groove range of 0 < x < 6:35(mm). The pressure values of the “end land" section are nil. This _field reveals the insignificance of the end land in the SFD characteristics even in the absence of an end seal. On the other hand, the seal groove contributes to the pressure field with a constant and non-zero pressure region. The magnitude of the pressure in this region is considerable. Hence, it can be concluded that the midland grooves enforce an axially constant and non-zero pressure field, contrary to the conventional perceptions. As was discussed before, pressure in the land zone is circumferentially varying. In the region between the two grooves, as is evident in Figs. 10 and 11, a linearly decreasing pressure zone associated with the land region exists. The pressure curve, especially for deeper supply grooves, exhibits a discontinuity where supply groove meets the land region. That is, a “pressure drop" takes place in the transition from large clearance of the supply groove to that of the land region. This phenomenon, which occurs due to the Bernoulli effect and inertia of the lubricant, resembles the pressure drop in flow restrictors. In general, the trend in Figs. 10 and 11 is the pressure decrease as the supply groove clearance GC decreases.

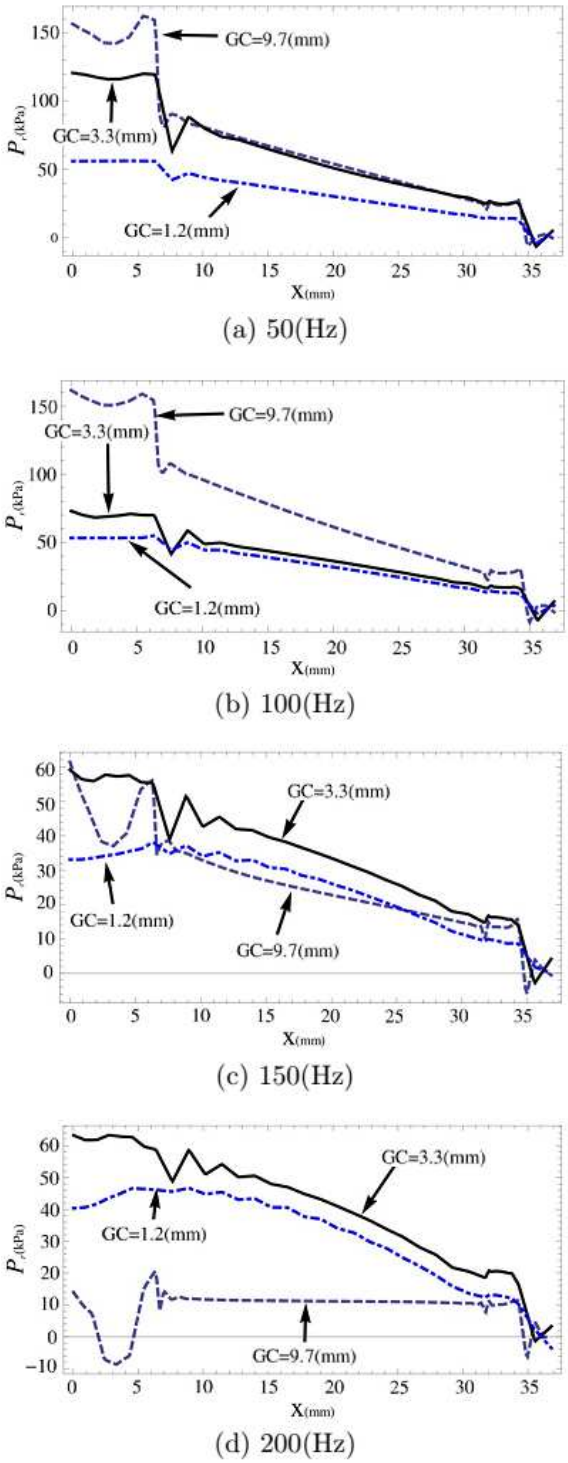

Fig. 10. Axial pressure profile on the journal surface at θ = 90', θ is measured from Y axis in Y,Z plane.

This significant observation is in contrast with the general realization practiced in industrial computer programs where the supply pressure is enforced at the edge of land region as a boundary condition. Figure 12 presents the variation of pressure in circumferential direction for the middle point of the land region.

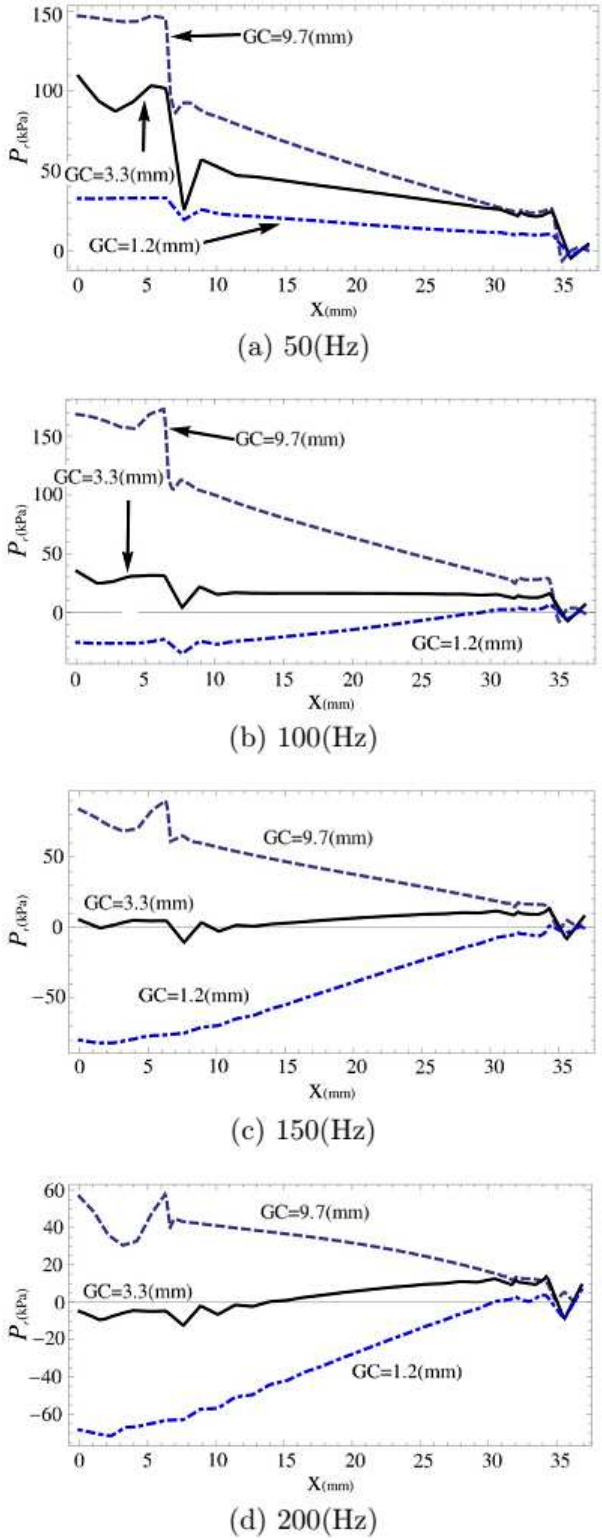

Fig. 11. Axial pressure profile on the journal surface at θ = 180', θ is measured from Y axis in Y,Z plane.

The conspicuous feature of these figures is the existence of three pressure zones with three peaks, similar to the three pressure zones in the supply groove shown in Fig. 8.

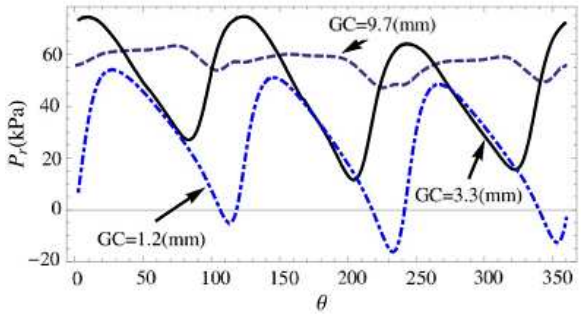

(a) 50(Hz)

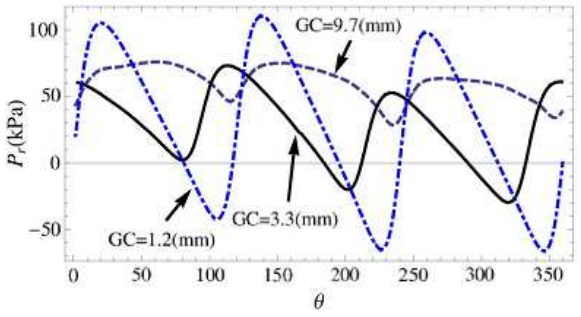

(b) 100(Hz)

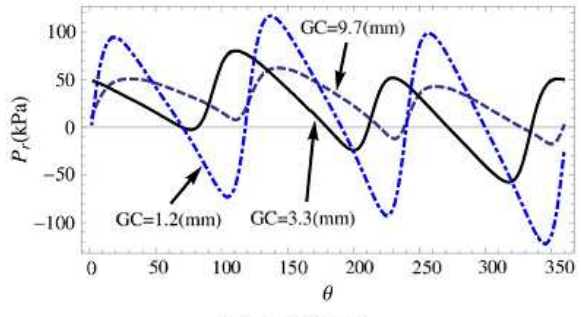

(c) 150(Hz)

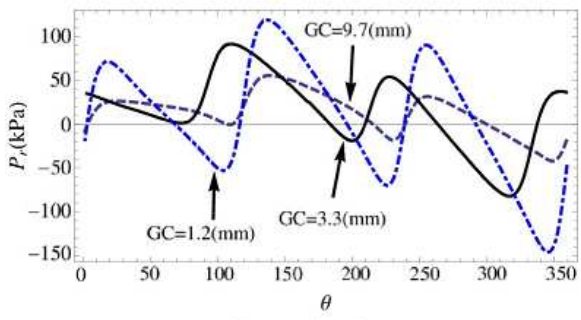

(d) 200(Hz)

Fig. 12. Circumferential pressure profile on the journal surface in the middle of the land region at X = 18(mm)

The obvious justification of such a pattern is the inlet holes arrangement. This pattern is not reported for a similar SFD with small clearance and low supply pressure in [3, 9]. In addition to the holes arrangement, the larger than usual clearance of the land, i.e., cl/R = 0.004 > 0.001, low eccentricity of CCO, and the high supply pressure, which dominates the hydrodynamic contribution of squeeze motion, contribute to the pressure pattern in the land region. Further investigations are required on this subject. In Fig. 12, effect of the supply groove clearance on the pressure profile developed in the land area is depicted, as well. It can be seen that the peak to peak pressure exhibits an inverse correlation with GC, that is, higher peak to peak pressure values are generated for lower GC values. This indicates the necessity of a deep supply groove for an effective pressurization. In other words, direct hole feeding to the land region, which is practiced in some designs, is a poor lubrication technique. In addition to the previous findings, Figs. 10-12 substantiate the negative pressure zones appearance and extension with the increase in the whirl speed despite the high supply pressure and large land clearance. Moreover, the comparison of the results of the cases with and without air entrainment shows that the variation of the SFD behavior is less than 5%, thus, it can be concluded that high pressure SFDs behavior is not susceptible to the ordinary air entrainment values.

VIII. Force Analysis

The developed hydrodynamic forces are obtained by integrating the pressure field developed on the journal. These forces naturally exhibit a nonlinear behavior with respect to the displacement and whirl speed. Nonetheless, approximating these forces with linearized coefficients for a pre-assumed trajectory, CCO in this study, is a common practice. Thus, for an assumed trajectory, one can write

$$\begin{bmatrix} M(\omega) & m(\omega) \\ -m(\omega) & M(\omega) \end{bmatrix}\begin{bmatrix} \ddot{y} \\ \ddot{z} \end{bmatrix}+\begin{bmatrix} C(\omega) & c(\omega) \\ -c(\omega) & C(\omega) \end{bmatrix}\begin{bmatrix} \dot{y} \\ \dot{z} \end{bmatrix} + \begin{bmatrix} K(\omega) & k(\omega) \\ -k(\omega) & K(\omega) \end{bmatrix}\begin{bmatrix} y \\ z \end{bmatrix}=\begin{bmatrix} -F_y(\omega) \\ -F_z(\omega) \end{bmatrix} \quad (6)$$

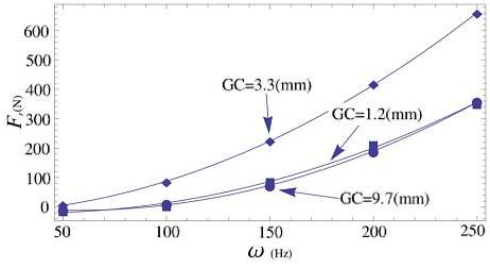

(a) radial force (Y direction)

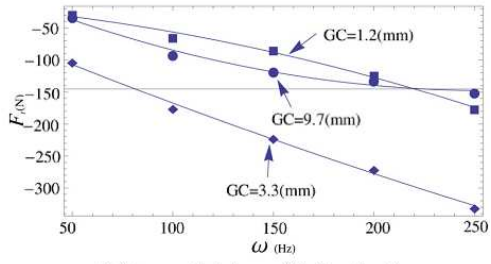

(b) tangential force (Z direction)

Fig. 13. Force variation of SFD versus whirl speed

Where

$$y = R\cos(\theta) \quad (7)$$

$$y = R\sin(\theta) \quad (8)$$

The position designated by $\theta = 0$ corresponds to the studied steady-state case, where the calculated radial and tangential forces match the Cartesian

Table 2: Linear force coefficients of SFD, Experimental data reported for principal X and Y direction [1], Traditional analytical model Eqs. 11,12 , *CFD

$GC(mm)$	$M(kg)$	$m(kg)$	$C(\frac{kg}{s})$
9.7†	$X = 11.9$ $Y = 12.7$	–	$X = 5220$ $Y = 6060$
9.7‡	1.61	–	1210.47
9.7*	10.01	0.50	8489.2
3.3*	11.40	−0.69	8285.8
1.2*	8.31	1.53	1612.7

$GC(mm)$	$c(\frac{kg}{s})$	$K(\frac{N}{m})$	$k(\frac{N}{m})$
9.7†	–	X = -500 $Y = 800$	–
9.7‡	–	–	–
9.7*	7232.3	−853.3	930.0
3.3*	−19.73	867.4	−1728
1.2*	3776.3	361.5	−618.9

ones, i.e., $F_y = F_r$ and $F_z = F_t$, as shown in Fig. 4. Substituting Eqs. 7 and 8 in Eq. 6, and by assuming a harmonic motion [14-23], we have

$$-\frac{F_r}{R} = -\omega^2 M + \omega c + K \quad (9)$$

$$-\frac{F_t}{R} = \omega^2 m + \omega C - k \quad (10)$$

which presents the radial and tangential forces with the linearized rotor dynamic coefficients. Figure 13 illustrates the variation of the radial and tangential forces versus whirl speed. In these figures the discrete data related to the five aforementioned speeds as well as their quadratic curve fits from which the linear force coefficients are obtained (based on Eqs. 9,10), are plotted. In these figures, the absolute values of the forces attributed to GC = 3:3 are higher than those of the other two speeds. This postulates the existence of an optimum groove clearance which renders the best performance of the SFD. Based on the traditional analytical analysis for centered squeeze film damper where the groove effects are neglected, the damping and added mass coefficients calculated for noncavitated, i.e., 2π film, are

$$C = 2\times 12\pi\mu L\left(\frac{R}{c}\right)^3\left[1-\frac{\tanh\left(\frac{L}{2R}\right)}{\frac{L}{2R}}\right] \quad (11)$$

$$M = 2\times\pi\rho\left(\frac{L}{c}\right)R^3\left[1-\frac{\tanh\left(\frac{L}{2R}\right)}{\frac{L}{2R}}\right] \quad (12)$$

where the coefficient 2 accounts for the two lands separated by the central feeding groove [1]. Table 2 lists the linear force coefficients obtained from a quadratic curve fitting and compares them with experimental data reported by San Andres [1] and the analytical model represented in Eqs. 11,12. The experimental data is obtained for low supply pressure of Ps = 0.55(bar), while the CFD model is obtained by enforcing Ps = 4.137(bar). The experimentally obtained cross-coupled values are not reported due to their insignificance. It seems that pressurization results in a considerable cross-coupled damping values. The direct damping and added mass values despite the supply pressure differences, however, are comparable and the stiffness values are much smaller than the centering spring stiffness that makes them ignorable. The CFD overestimates the damping coefficient by 30% and underestimates the added mass by 20%, which can be attributed to the different supply pressure values. As is shown in Fig. 12, for the deepest groove, i.e., GC = 9.7, the cavitation is suppressed almost for all the excitation cases and negative pressure does not appear. This indicates the effectiveness of the pressurization in removing the cavitation in _lm land once deep groove is used, as mentioned before. Both experimental and CFD results deviate from the analytical model in Eqs. 11, 12 significantly. This is mainly due to the falsified traditional assumption that the supply groove isolates the land regions, while our results in Fig. 11 along with others' show that this region contributes to the dynamic pressure generation and in fact links the two adjacent lands. Hydrodynamic damping is the most important characteristic of a SFD. The principle damping related to GC = 9:7 and GC = 3:3 cases are almost the same, while GC = 9:7 has much higher cross-coupled damping content. This value is five times lower for GC = 1.2. On the other hand, the cross coupled damping is the highest for GC = 9.7. This finding shows, in contrary to the SFDs' traditional design perception, the importance of supply groove on the dynamic behavior of SFDs and its significance in their proper design. In the lack of journal rotation in SFDs, adoption of a centering element for lift-off_ and centering the motion is prevalent in industrial applications. The centering spring stiffness, which equals to Ks = 18:7(MN=m) in the related test rig reported in [3], often dominates the hydrodynamic ones generated by the whirl motion of the journal in housing. In the lack of centering element, the assumption of CCO is no longer valid [2]. It can be seen that the reported stiffness values in Table 2 are significantly smaller than that of the centering spring and can be ignored. The direct stiffness value of GC = 9.7 is a negative, while its absolute value is almost equal to the one with GC = 3.3. GC = 1.2 exhibits the lowest stiffness values as well as the damping ones

compared the other two study cases. SFDs, reportedly, exhibit a considerable amount of lubricant added mass [13, 14]. It is shown in Table 2 that the direct mass values of GC = 9:7 and GC = 3:3 are almost equal, and a 20% decrease occurs by reducing the GC value to 1:2(mm). It is also shown that the cross-coupled added mass increases as GC decreases. Note that based on Eq. 9 the stiffness restoring force and inertia forces oppose each other and in SFDs, the inertia forces are dominant.

IX. Summary and Conclusion

In this paper, a CFD analysis is conducted on an open end, large clearance, and centrally grooved SFD lubricated with high supply pressures. The results are obtained with CCO trajectory assumption for a range of whirl speeds. The lubricant is assumed to contain 4% entrained air, modeled as ideal gas and dispersed fluid. The result obtained in this paper can be summarized as follows

- The groove regions are characterized with vortex pattern flows with a considerable velocity in circumferential direction opposite to the journal whirl direction.
- The flow rate decreases with the increase in the whirl speed due to the higher pressures developed on the inlet holes. Decreasing the groove depth in general results in a decrease in a decrease in flow rate, as well.
- The supply groove is identified with a three-sector pressure zone separated by inlet holes. Due to the circumferential flows in the groove, the average pressure in this region is considerably lower than the supply one. The supply groove pressure variation in axial and radial direction is nil compared to the circumferential direction. This is in contrary with the traditional understanding of the SFDs' behavior, which considers the pressure in supply groove constant and equal to the inlet hole pressure.
- Considerable pressure is developed in seal groove, which is in the same order of magnitude of the neighboring land pressure. The pressure in this region is varying circumferential direction and not in axial direction.
- Pressure profile, in its positive region, exhibits the highest values at the supply groove. The land region is identified with an axially decreasing pressure profile. The seal groove region has axially almost constant pressure values and end land region exhibits atmospheric pressure content. In circumferential direction, the three-zone pressure pattern, observed in supply groove, appears similarly in the land region, as well.
- Despite the pressurization, negative pressure zone and cavitation occurs for higher whirl speeds and shallow supply groove cases. This makes multi solution and jump phenomenon probable, even for the pressurized SFDs.
- The obtained hydrodynamic forces, both in radial and tangential directions, show the highest values for GC = 3.3. This postulates an optimum groove depth for which SFD is the most effective. It can be inferred that to have an effective lubrication free from negative pressure zones and relatively uniform pressure in circumferential direction, deeper supply grooves are required.
- The linear coefficients of the case with GC=9.7 are validated with experimental data. This experimentally obtained data, although obtained for a lower supply pressure, show that our CFD results are correct and in the expected magnitude.
- The linearized coefficients in general does not show a predictable variation pattern with groove depth change. Study cases with GC=9.7 and GC=3,3 exhibit very close direct damping values as the most important characteristic of SFDs. By decreasing GC from 9.7 to 3.3, the lubricant added mass coefficient increases, but with a further decrease to 1.2, it plummets.

In general, it can be concluded that the supply groove and the supply holes arrangement have nonlinear effects on the dynamic of SFDs. Although the use of CFD analyses has become prevailing in industry, a majority of designs rely on Reynolds based analysis and computer programs which may oversimplify the problem. Further CFD studies on the subject of supply 22 groove and holes arrangement and their dynamic can provide insight in how to model their behavior better in Reynolds equation based solvers.

References

[1] L. San Andres, (2014). Force coefficients for a large clearance open ends squeeze film damper with a central feed groove: Experiments and predictions. Tribology International, 71, 17-25.

[2] S., Dousti, T.W., Dimond, P.E., Allaire, H.E., Wood, (2013). Time Transient Analysis of Horizontal Rigid Rotor Supported With O-Ring Sealed Squeeze Film Damper, ASME 2013, International Mechanical Engineering Congress and Exposition.

[3] L. San Andres, (2012), Damping and Inertia Coefficients for Two Open Ends Squeeze Film Dampers with a Central Groove: Measurements and Predictions", Proc. of ASME IGTI TurboExpo, GT2012-6212.

[4] S., Dousti, J.A., Kaplan, F., He, P.E., Allaire, (2013), Elastomer O-Rings as Centering Spring in Squeeze Film Dampers: Application to Turbochargers, ASME Turbo Expo 2013: Turbine Technical Conference and Exposition, 2.

[5] J.I., Inayat-Hussain, H., Kanki, N.W., Mureithi, (2003), On the bifurcations of a rigid rotor response in squeeze –film dampers, Journal of Fluids and Structures, 17, 3, pp. 433-459.

[6] J. Y., Zhao, and E. J., Hahn, (1993), Subharmonic, quasi-periodic and chaotic motions of a rigid rotor supported by an eccentric squeeze film damper, IMechE, Proc Inst Mech Engrs,, Part C: J. Mechanical Engineering Science, 207, pp. 383-392.

[7] F., Zeidan, and J., Vance, (1990), Cavitation and Air Entrainment Effects on the Response of Squeeze Film Supported Rotors, ASME Journal of Tribology, 112, pp. 347-353.

[8] F., Zeidan, and J., Vance, (1990), Cavitation Regimes in Squeeze Film Dampers and Their Effect on the Pressure Distribution", Tribology Transactions, 33, (3) pp. 447-453.

[9] P., Boppa, G., Morrison, and A., Sekaran, (2013), A Numerical Study of Squeeze Film Dampers", Proc of ASME TurboExpo 2013, GT2013-95547, June 3-7, 2013, San Antonio, Texas, USA.

[10] S., Simandiri, and E. J., Hahn, (1976), Effect of Pressurization on the Vibration Isolation Capability of Squeeze Film Bearings, Journal of Engineering for Industry, 98, Series B, N.1 , pp. 109-117.
[11] S., Dousti, J., Cao, A., Younan, P., Allaire, and T., Dimond, (2012), Temporal and Convective Inertia Effects in Plain Journal Bearings With Eccentricity, Velocity and Acceleration, Journal of Tribology, 134, pp.174-184.
[12] L., San Andrs, and A. Delgado, (2012). A Novel Bulk-Flow Model for Improved Predictions of Force Coefficients in Grooved Oil Seals Operating Eccentrically. Journal of engineering for gas turbines and power, 134(5).
[13] J. W., Lund, C. M., Mylleup, and H., Hartman, (2003), Inertia Effects in Squeeze-Film Damper Bearings Generated by Circumferential Oil Supply Groove, Journal of Vibration and Acoustic, 125, (4), pp. 495-499.
[14] S., Dousti, (2014), An Extended Reynolds Equation Development with Applications to Fixed Geometry Bearings and Squeeze Film Dampers, Ph.D. dissertation, University of Virginia, Charlottesville, Virginia, USA.
[15] S., Dousti, and M.A., Jalali, (2013), In-Plane and Transverse Eigenmodes of High-Speed Rotating Composite Disks, Journal of Applied Mechanics, 80(1), p.011019.
[16] S., Dousti, and R.L., Fittro, (2015), An Extended Reynolds Equation Including the Lubricant Inertia Effects: Application to Finite Length Water Lubricated Bearings, Proc. of ASME TurboExpo 2015, GT2015- 43826, June 15-19, 2015, Montreal, Canada.
[17] S., Dousti, (2012), Realistic Squeeze Film Damper Analysis: Application of Gas Turbines Engines, Rotating Machinery and Controls Consortium (ROMAC) Annual Meeting, Charlottesville, VA, USA.
[18] J. A., Kaplan, S., Dousti, P. E., Allaire, B. R., Nichols, T. W., Dimond, A. Untaroiu, (2013), Rotor Dynamic Modeling of Gears and Geared Systems. In ASME Turbo Expo 2013: Turbine Technical Conference and Exposition.
[19] E., Sarshari, N., Vasegh, M., Khaghani, S., Dousti, Sliding Mode Control in Ziegler's Pendulum With Tracking Force: Novel Modeling Considerations, ASME 2013 International Mechanical Engineering Congress and Exposition (2013).
[20] M. Y. Abdollahzadeh Jamalabadi, and S., Dousti, (2015), Feasibility study of magnetic effects on silver nanoparticles for drug and gene delivery in Cyprinus carpio Journal of Chemical and Pharmaceutical Research, , 7(12):206-218.
[21] A., Gerami, P., Allaire, and R. Fittro, (2015). Control of Magnetic Bearing With Material Saturation Nonlinearity. Journal of Dynamic Systems, Measurement, and Control,137(6), 061002.
[22] A., Gerami, P., Allaire, and R., Fittro, (2014). Nonlinear Modeling and Control of a Magnetic Bearing with Material Saturation, Proceedings of the 14th International Conference on Magnetic Bearings, Linz, Austria.
[23] A., Sakhaee-Pour, A. Gerami, and A., Ahmadian, (2008). Development of an equation to predict radial modulus of elasticity for single-walled carbon nanotubes. Proceedings of the Institution of Mechanical Engineers, Part C: Journal of Mechanical Engineering Science, 222(6), 1109-1115.

AUTHOR'S PROFILE

Saeid Dousti is a Senior Technical Fellow at Rotor Bearing Solutions International, Charlottesville, Virginia, USA.

Ali Gerami is a control systems engineer at Wrightspeed, San Jose, California, USA.

Majid Dousti is a research assistant at faculty of engineering, Zanjan University, Zanjan, Iran.